A general model for welding of ash particles in volcanic systems validated using *in situ* x-ray tomography

Fabian B. Wadsworth[1,2,3], Jérémie Vasseur[3], Jenny Schauroth[4], Edward W. Llewellin[1],

Katherine J. Dobson[1], Tegan Havard[1], Bettina Scheu[3], Felix W. von Aulock[4],

James E. Gardner[5], Donald B. Dingwell[2,3], Kai-Uwe Hess[3], Mathieu Colombier[3],

Federica Marone[6], Hugh Tuffen[7], Michael J. Heap[8]

[1]Department of Earth Sciences, Durham University, Durham, DH1 3LE, U.K. [2]Centre for Advanced Study, Ludwig-Maximilians-Universität, Munich, Germany. [3]Department of Earth and Environmental Science, Ludwig-Maximilians-Universität, Theresienstr. 41, Munich 80333, Germany. [4]School of Environmental Sciences, University of Liverpool, Jane Herdman Building, Liverpool L69 3GP, U.K. [5]Department of Geological Sciences, Jackson School of Geosciences, 2305 Speedway Stop C1160, Austin, TX 78712-1692, U.S. [6]Swiss Light Source, Paul Scherrer Institut, 5232 Villigen PSI, Switzerland. [7]Lancaster Environment Centre, Lancaster University, LA1 4YQ, U.K. [8]Institut de Physique du Globe de Strasbourg (UMR 7516 CNRS), Université de Strasbourg, 5 rue René Descartes, F-67084, Strasbourg, France.

sintering; porosity; synchrotron; surface tension; tomography; tuffisite; jet engine; obsidian

corresponding author: fabian.b.wadsworth@durham.ac.uk

Abstract:

Welding occurs during transport and deposition of volcanic particles in diverse settings, including pyroclastic density currents, volcanic conduits, and jet engines. Welding rate influences hazard-relevant processes, and is sensitive to water concentration in the melt. We characterize welding of fragments of crystal-free, water-supersaturated rhyolitic glass at high temperature using *in-situ* synchrotron-source x-ray tomography. Continuous measurement of evolving porosity and pore-space geometry reveals that porosity decays to a percolation threshold of $1-3$ vol.%, at which bubbles become isolated and welding ceases. We develop a new mathematical model for this process that combines sintering and water diffusion, which fits experimental data without requiring empirically-adjusted parameters. A key advance is that the model is valid for systems in which welding is driven by confining pressure, surface tension, or a combination of the two. We use the model to constrain welding timescales in a wide range of volcanic settings. We find that volcanic systems span the regime divide between capillary welding in which surface tension is important, and pressure welding in which confining pressure is important. Our model predicts that welding timescales in nature span seconds to years and that this is dominantly dependent on the particle viscosity or the evolution of this viscosity during particle degassing. We provide user-friendly tools, written in Python™ and in Excel™, to solve for the evolution of porosity and dissolved water concentration during welding for user-defined initial conditions.

Key points:

    (1) First *in situ* determination of the welding rates of hydrous magma.

    (2) A new mathematical model that couples volatile mass transfer with welding kinetics.

    (3) This work provides a model relevant for ignimbrite and tuffisite welding

1. Introduction

Magma fragments into particles during explosive volcanic activity. Subsequent welding of these particles can occur at the base of hot pyroclastic density currents (Walker 1983; Branney et al. 1992), at the walls of volcanic conduits (Gonnermann and Manga 2003; Rust et al. 2004; Gardner et al. 2017), in tuffisite veins (Tuffen et al. 2003; Kendrick et al. 2016; Gardner et al. 2018), in the hot zone of jet engines (Giehl et al. 2016), and when lightning strikes volcanic ash in the air or on the ground (Cimarelli et al. 2017; Mueller et al. 2018). Despite this wide range of welding scenarios, there has been little work on the physics of welding of volcanic droplets, beyond simple empirical, semi-empirical, or scaling approaches (Friedman et al. 1963; Riehle 1973; Sparks et al. 1999; Quane and Russell 2005a; Russell and Quane 2005; Vasseur et al. 2013; Wadsworth et al. 2014).

Welding involves a reduction of inter-particle pore space (Branney and Kokelaar 1992; Sparks et al. 1999; Quane and Russell 2005a; Vasseur et al. 2013). Porosity is therefore a convenient metric for tracking the degree of welding, and has been used to rank the 'grade' of a welded deposit (Quane and Russell 2005b; Wright and Cashman 2014). Theoretical models for the evolution of porosity as a function of time in a welding system have been proposed (Frenkel 1945; Mackenzie and Shuttleworth 1949) but they do not account for the complexities of welding in magmatic systems, which include non-isothermal behavior, disequilibrium of dissolved volatile species, and the effect of a confining pressure that pushes the particles together. Non-isothermal behavior is important because welding in nature may occur as the particles cool (e.g. at conduit margins, within ejected ballistic bombs, or in ignimbrites) or follow more complex heating and cooling pathways (e.g. in a jet engine). Disequilibrium of volatile species – particularly of water – is important because the solubility changes as the pressure and temperature environment of the particles changes, driving diffusion in or out of the particles during welding (Sparks et al. 1999; Gardner et al. 2018). In the case of water, this

67 has a strong impact on the viscosity of the particle (Hess and Dingwell 1996) affecting welding

68 rate (Grunder et al. 2005; Gardner et al. 2018, 2019). Confining (or lithostatic) pressure

69 resulting, for example, from the weight of aggrading particles at the base of a pyroclastic

70 density current, is important because it provides a stress that pushes the droplets together,

71 accelerating welding. Previous theoretical and quantitative models for welding have focused

72 on cases where welding is driven by surface tension alone (Wadsworth et al. 2016) or, where

73 pressure is considered, have relied on scaling arguments (Sparks et al. 1999) or purely

74 empirical correlations (e.g. Riehle 1973).

75 We develop a general and versatile mathematical framework for welding that can be used

76 to predict the textural evolution of a welding pack of particles in a wide range of natural

77 settings. We perform and analyze experiments conducted under non-isothermal, disequilibrium

78 conditions to validate the model.

79

80 **2. A theoretical model for droplet welding dynamics**

81 **2.1 Viscous welding under arbitrary pressure**

82 Previous work on non-volcanic welding (or 'sintering') of spherical particles has shown that

83 in the viscous state (i.e. when particles are droplets), surface-tension-driven welding is well

84 described by a 'vented bubble model', in which the inter-droplet porosity is abstracted as a

85 system of spherical bubbles in liquid shells, which are 'vented' so that the gas can escape as

86 the bubbles shrink (Mackenzie and Shuttleworth 1949; Wadsworth et al. 2016). The geometric

87 assumptions of the vented bubble model are most valid for highly polydisperse particle

88 distributions (Wadsworth et al. 2017b) of the sort typical in nature, and the approximation

89 becomes increasingly accurate as welding progresses because, as the droplets coalesce, the

90 microstructural geometry continuously diverges from 'droplet-like' towards 'bubble-like' –

91 that is, there is a topological inversion of the pore space (Wadsworth et al. 2017a). We start

92   from the assumption that the vented bubble model also applies to initially-angular particles.

93   The conceptual steps in the geometric abstraction from an ash pack to a system of vented

94   bubbles are shown in Figure 1.

95   We extend the vented bubble model to include a confining pressure that acts alongside

96   surface tension stress to drive welding, where we use the term *confining* pressure to refer to an

97   isotropic pressure acting to push the particles together – equivalently, when viewing the

98   particles as viscous droplets, an isotropic pressure in the continuous liquid phase of the

99   coalescing droplets. In their supplementary material, Wadsworth et al. (2016) derive the vented

100   bubble model from the model of Prousevitch et al. (1993) for bubble growth in magma by

101   setting the bubble pressure inside the associated liquid shell to be equal to the gas pressure

102   outside the shell at all times. Here, we relax that assumption, and instead set the pressure

103   difference to a value ΔP. Neglecting inertia, the full equation for the inter-droplet porosity ϕ

104   with time t is then

105

$$\frac{d\phi}{dt} = -\frac{3\Delta P}{4\mu}\phi - \frac{3\Gamma}{2\mu a_i}\left(\frac{\phi_i}{1-\phi_i}\right)^{1/3}\phi^{2/3}(1-\phi)^{1/3},$$

Eq. 1

106

107   where ΔP is the difference between the confining pressure on the liquid droplets P_l and the

108   pressure of the interstitial gas P_g, such that $\Delta P = P_l - P_g$, μ is the particle viscosity, Γ is the

109   interfacial tension between the particles and the gas, a_i is the initial size of the bubble, and ϕ_i

110   is the initial porosity when welding starts. A derivation of Eq. 1 from the Rayleigh-Plesset

111   equation is given in the Supplementary Information.

112   Eq. 1 can be cast in dimensionless form by normalizing time to a characteristic capillary

113   timescale $\lambda = \mu a_i/\Gamma$, such that $\bar{t} = t/\lambda$, normalizing pressure to a capillary pressure scale $P_c =$

114   $2\Gamma/a_i$, such that $\bar{P} = \Delta P/P_c$, and normalizing porosity to its initial value, such that $\bar{\bar{\phi}} = \phi/\phi_i$,

115   yielding

116

$$\frac{d\bar{\phi}}{d\bar{t}} = -\frac{3}{2}\left[\bar{P}\bar{\phi} + \left(\frac{1 - \phi_i\bar{\phi}}{1 - \phi_i}\right)^{1/3}\bar{\phi}^{2/3}\right],$$

Eq. 2

117

118   where a bar above a parameter denotes that it has been rendered dimensionless. The first term

119   within the square brackets represents the contribution of the confining pressure, the second

120   term represents the contribution of the capillary (Laplace) pressure.

121   The dimensionless time $\bar{t}$ can be generalized to account for non-isothermal

122   temperature–time history, which is especially useful for natural magmatic scenarios. This is

123   achieved by accounting for the change in viscosity μ as temperature varies, via

124

$$\bar{t} = \frac{t}{\lambda} = \frac{\Gamma}{a_i}\int_{t_i}^{t}\frac{1}{\mu}dt$$

Eq. 3

125

126   where t_i is the time at which the welding process starts. In casting Eq. 3 this way, we assume

127   that Γ is a constant, independent of time during welding. In reality, Γ is dependent on both

128   water concentration and temperature, however, variations in surface tension are negligible

129   compared with variations in liquid viscosity arising from the effects of both temperature and

130   water concentration (discussed later). Together, Eqs 2 & 3 represent a universal description of

131   isotropic, viscous particle welding, derived from micromechanical first principles. In the case

132   where $\bar{P} = 0$, this approach has been validated against experimental data across a large range

133   of temperatures (Wadsworth et al. 2016). While other models exist, they are either less easy to

134   use, requiring a switch-point between two competing processes (Prado et al. 2001), or they rely

135   on bulk properties of the system, which have to be empirically determined and are therefore

136   less general as they are not constructed from the micromechanics involved (Olevsky 1998;

137   Quane and Russell 2005a).

138   The parameter a_i can be difficult to measure, or even define, for what is a complex,

139   interconnected pore network (Figure 1). We use a relationship between a_i and the distribution

140   of particle sizes $F(R)$ in a pack of particles or droplets (Lu and Torquato 1992), which is

141   described in detail elsewhere (Wadsworth et al. 2016, 2017b). The relationship relies on

142   knowledge of ϕ_i, and the moments of the distribution of R, denoted $\langle R^n \rangle$, which can be

143   grouped into a polydispersivity factor $S = \langle R \rangle \langle R^2 \rangle / \langle R^3 \rangle$. The output from this is a pore size

144   distribution $f(a_i)$ that relates to the particle size distribution $F(R)$ and ϕ_i, and is described in

145   the Supplementary Information along with an account of how this is used in conjunction with

146   Eqs 1-2 using convolution techniques (Wadsworth et al. 2017b).

147

148   **2.2 Accounting for diffusion of volatiles during welding**

149   In the model formulation above, the viscosity μ is assumed to be dependent on temperature, T,

150   only. However, viscosity also depends on the concentration of water dissolved in the melt,

151   which, in nature, may vary during welding. Volcanic particles formed at fragmentation may be

152   super-saturated in dissolved water (Giachetti and Gonnermann 2013), and that super-saturation

153   can grow as the particles ascend rapidly to lower pressures up-conduit without time to fully re-

154   equilibrate (Gardner et al. 2017). Similarly, the solubility of water increases as the particles

155   cool, which may cause them to re-hydrate (McIntosh et al. 2014; Ryan et al. 2015). Mass

156   diffusion of water in or out of particles may occur on timescales similar to the timescale of

157   welding (Sparks et al. 1999; Gardner et al. 2017, 2018, 2019); consequently, we anticipate that

158   diffusion of water can affect the rate of welding through its impact on melt viscosity.

159   In order to account for diffusion, we must define the geometry of the internal welding

160 system. The internal geometry of welding systems is complex and evolves from an initial state

161 of particles in a gas continuum, to bubbles isolated in a liquid continuum. A rigorous solution

162 for mass diffusion through this evolving geometry would require an approach that explicitly

163 resolves both the fluid motion and the diffusion. However, as for the welding model, we

164 simplify the problem by abstracting the geometry. For the purposes of diffusion modeling we

165 assume that the particles remain spherical and simply apply Fick's 2nd law in spherical

166 coordinates,

167

$$\frac{\partial C}{\partial t} = \frac{1}{r^2}\frac{\partial}{\partial r}\left(r^2 D \frac{\partial C}{\partial r}\right),$$

                    Eq. 4

168

169 where C is the concentration of water in the melt particle, D is its diffusivity (which depends

170 on temperature and local water concentration), and r is the radial position from the particle

171 center. We adopt the assumption that the initial concentration of dissolved water C_i is uniform

172 throughout the particle at the onset of welding, giving the initial condition $C = C_i$ for all r at

173 $t = 0$. At all later times the water concentration at the surface of the particle is given by the

174 equilibrium solubility C_e at the current conditions of gas pressure P_g and temperature T, giving

175 the boundary condition $C = C_e(t)$ at $r = R$ for $t > 0$. We define a zero-flux boundary

176 condition at the center of the particle: $\partial C/\partial r = 0$ at $r = 0$.

177   To account for the effect of variable water concentration in the particle we determine a

178 spatial average by integrating C over $0 < r < R$; this integral is $\langle C \rangle = \int_0^1 C \, d\bar{r}$, where $\bar{r} =$

179 r/R. We then use $\langle C \rangle$ to compute an average viscosity $\langle \mu \rangle$ which is used in Eqs 1-3 in place of

180 μ. This approach results in an effective coupling between the diffusion model (Eq. 4) and the

181 welding model (Eqs 1-3). In the Supplementary Information, we describe the numerical

182   solution of these equations in detail. We note here that our assumption of spherical particles

183   undergoing diffusion of volatiles may be invalid at large polydispersivity for cases where the

184   smallest particles are in equilibrium while the largest particles are far from equilibrium. This

185   is discussed elsewhere (Gardner et al. 2019).

186

187   **3. Experimental validation: materials and methods**

188   Our starting material is a metaluminous, tholeiitic natural rhyolitic glass collected from

189   Hrafntinnuhryggur, Krafla (Iceland). We crushed the obsidian to a powder using an agate

190   mortar and pestle and then crushed the resultant chips to a fine powder using a concussion ball

191   mill for short durations to prevent the sample heating significantly. The powder was sieved to

192   < 125 μm diameter pieces and the size distribution was measured using a Beckman Coulter

193   LS™ 230 laser refraction particle size analyzer with the measuring range $0.375 - 1000$ μm

194   diameter. The particle size distribution is given in the Supplementary Information, and has a

195   mean radius $\langle R \rangle = 2.2 \times 10^{-5}$ m.

196   Using a Netzsch Pegasus 404c device for simultaneous thermal analysis, we determined

197   the dissolved volatile concentration that is excess (above solubility) at up to 1325 K to be $C_i =$

198   0.15 ± 0.02 wt.%, by the relative loss of mass during heating, consistent with Tuffen and

199   Castro (2009). This determination was performed on single chips ($n = 6$) from within a few

200   millimeters of the sub-sample of the glass block that was used throughout this study.

201   To solve the governing equations given in our model, we require a parameterization for

202   D, μ, and C_e relevant to the material in question. We use models relevant to the metaluminous

203   rhyolites (Hess and Dingwell 1996; Liu et al. 2005; Zhang and Ni 2010)

204

$$\log_{10}(\mu) = -3.545 + 0.833 \ln(C) + \frac{9601 - 2368 \ln(C)}{T - 195.7 - 32.25 \ln(C)}$$

$$D = C \exp\left[-18.1 + 0.001888P_l - \left(\frac{9699 + 3.626P_l}{T}\right)\right]$$

Eq. 5

$$C_e = \frac{354.941P_w^{0.5} + 9.623P_w - 1.5223P_w^{1.5}}{T} + 0.0012439P_w^{1.5}$$

205

206   where P_w is the partial pressure of water in the interstitial gas phase, and the coefficients given

207   are valid when T is in K, P_l and P_w are in MPa, and C and C_e are in wt.%. In the Supplementary

208   Information we independently verify $\mu(T)$ for our material using a parallel plate compression

209   method (Hess et al. 2007), a calorimetric method using a shift factor of 10.4 (Gottsmann et al.

210   2002), and a micropenetration method (Hess et al. 1995), which all demonstrate internal

211   consistency, as well as matching the prediction of Eq. 5 for the measured C_i. We take a value

212      $P_w = P_l\alpha$ with $\alpha = 0.2$, representing the typical humidity pressure in a laboratory furnace.

213   Finally, we use $\Gamma = 0.3$ N.m^{-1}.

214   We performed two sets of *in situ* high temperature experiments, which used different

215   methods to image the evolution of a welding pack of obsidian powder, lightly pressed into a

216   free-standing cylinder with 3 mm diameter: (1) synchrotron-source x-ray tomography,

217   providing continuous 3-dimensional microstructural data; and (2) optical dilatometry,

218   providing bulk sample volume changes only. The first set of experiments were performed at

219   the TOMCAT beamline of the Swiss Light Source at the Paul Scherer Institute. Cylinders of

220   obsidian powder were loaded into the imaging window of the x-ray beam path. We used a laser

221   system (Fife et al. 2012) to heat an alumina sleeve (muffle) placed over the samples, thus

222   heating the obsidian pack indirectly. The temperatures measured by a pyrometer were

223   calibrated by comparing the *in situ* welding of a well-studied sample of monodisperse glass

224   beads with *ex situ* characterization of the same process (Wadsworth et al. 2016), resulting in a

225   continuous correction for T, and confirming that temperature gradients on the sample scale

226   were negligible. Full 3-dimensional tomographs were collected at 5.5×10^{-3} Hz with a spatial

227 resolution of 1.6 μm. The second set of experiments were performed using a Hesse Instruments

228 EM-201 optical dilatometer, which continuously records the silhouette of the sample during

229 heating at 1 Hz. Volume is determined from the silhouette as the solid of revolution.

230   The experiments covered a wide range of conditions, including isothermal

231 experiments at temperatures of $1050 - 1500$ K, and linear heating ramps at rates of $0.04 -$

232 $0.25\,\mathrm{K.s^{-1}}$.The data from optical dilatometry are confined to porosity $\phi(t)$, while the

233 tomography provides 3-dimensional data that are used to measure both the total porosity $\phi(t)$,

234 and the porosity that is connected across the sample (or segmented domain) $\phi_p(t)$. After the

235 heating experiments, we repeated the thermal analysis step on a few sub-samples, and no mass

236 loss was observed, demonstrating the samples did equilibrate volatiles during the *in situ*

237 experiments.

238   Supplementing our datasets collected at relatively low C_i and a small difference

239 between C_i and C_e (small initial supersaturation), we re-analyse the data from Gardner et al.

240 (2018) and Gardner et al. (2019). These data were collected at high P_g such that the equilibrium

241 water concentration is also high. These data also include particles that hydrate and particles

242 that de-hydrate while also welding.

243   All of the above experiments were conducted without confining pressure, hence $\bar{P} \approx 0$, a

244 situation typical of small-scale laboratory settings. In order to examine the effect of $\bar{P} > 0$, we

245 use data for welding Pyrex™ glass presented previously (Friedman et al. 1963). In those

246 experiments the glass was crushed to a particle size around $100 - 250$ μm (not specified

247 exactly), and welded under a uniaxial liquid pressure of $P_l = 1.52 \times 10^6$ Pa and $P_l = 3.63 \times$

248 10^6 Pa at temperatures $883 - 943$ K. We re-analyze these data using our model. While the

249 same authors provide data for rhyolite particle welding (Friedman et al. 1963), some doubt

250 exists as to the exact pressures used (Sparks et al. 1999) so we choose not to reanalyze those

251 data.

252

4. Results, data analysis and model validation

In situ tomography allows us to render the evolving internal pore space of the samples in 3-dimensions through the welding process. Figure 2 shows a typical experimental result. The pore space is initially fully interconnected, and has a complex geometry between the angular glass fragments. As we heat the sample, the glass particles relax to liquid droplets at high temperature, and the droplet–droplet contacts weld. The porosity decreases with time smoothly and monotonically, and the rate at which it decreases depends strongly on temperature (in the isothermal experiments) or heating rate (in the non-isothermal experiments). The connectivity of the pore space drops during welding from fully connected at the start ($\phi_p/\phi = 1$), to fully closed at volume equilibrium ($\phi_p/\phi = 0$). The porosity at which the connectivity drops to zero is the percolation threshold porosity ϕ_c below which the system is impermeable. We determine this from our experiments as $\phi_c = 0.02 \pm 0.019$, which agrees with theory, simulations (Elam et al. 1984; Vasseur and Wadsworth 2017), and experiments (Wadsworth et al. 2016) in other welding droplet or overlapping sphere systems. This value is far lower than the percolation threshold for bubbly systems, as has previously been noted for the internal geometry of welding systems (Vasseur and Wadsworth 2017).

In Figures 2g & 3, we compare the results for the *in situ* x-ray tomography and optical dilatometry experiments with the model presented in section 2. For these unconfined laboratory-scale tests, the value of $\bar{P}$ is effectively 0. For the isothermal experiments we solve Eq. 2 with $\bar{P} = 0$, accounting for the diffusion of water out of the particles during welding via Eqs 3 & 4 (Figures 3a & 3b). For the non-isothermal experiments we additionally account for temperature change via Eq. 3 (Figure 3c). In both cases, we find good agreement and a reasonable collapse of the data to the model. This result highlights that, in these experiments, welding rates are influenced by temperature and volatile content, both of which control the

277   particle viscosity and can evolve on the same timescale as the welding; hence, they must be

278   solved explicitly (Eqs 3 & 4). Welding rate also depends on particle size distribution, interfacial

279   tension, and the initial porosity of the packed particles. Particle angularity may subtly affect

280   both the diffusion rate and the sintering rate when compared with the model, which is based on

281   idealised spherical particles, but, given the good agreement between model and data, this effect

282   does not appear to be of first-order.

283   The experimental validation of our simple model for $\bar{P} = 0$ appears to be successful. To

284   extend this to conditions where $\bar{P} > 0$, we re-analyse the results from Friedman et al. (1963)

285   in which anhydrous glass was heated under pressure. In the Supplementary Information we

286   give a detailed description of the methods used in Friedman et al (1963), but note here that Eqs

287   1 and 2 are valid in their experiments. We assume that the uniaxial nature of their applied loads

288   can be accounted for using the Trouton ratio, such that our model for isotropic pressurization

289   can be adapted to uniaxial conditions. For their anhydrous experiments, conducted at $\bar{P} = 100$,

290   we apply Eq. 2 directly. We find good agreement across a wide range of temperature (Figure

291   4), validating our model up to naturally relevant pressures and across the regime boundary $\bar{P} =$

292   1. These conditions represent the state where the volcanic particles are under pressure, but the

293   interconnected gas phase between the particles remain un-pressurized, which is a typical

294   scenario for larger systems in nature. We show that, in this case, the time required for welding

295   to complete is reduced by the elevated confining pressure, as implied by Eq. 2 (note how the

296   data collapse to a model curve to the left of the $\bar{P} = 0$ curve in Figure 4, and are therefore

297   welding more rapidly).

298

299   **5. Discussion**

300   **5.1 Validity of the welding model**

301   The welding model agrees well with experimental data across a wide range of conditions,

302   validating the model for application to welding systems: 1) with and without applied pressure;

303   2) under isothermal and non-isothermal conditions; 3) in which dissolved water is in

304   equilibrium or disequilibrium with ambient pressure and temperature conditions. Thus the

305   model is sufficiently general to capture most of the essential features of welding scenarios in

306   magmatic and volcanic systems. There are, however, two limitations. Firstly, the model does

307   not apply directly to welding under high shearing stress. We do use experimental data in which

308   welding particles are under uniaxial compression (Friedman et al. 1963), such that the

309   anisotropy of the pressure applied results in shear stresses internal to the sample (c.f. uniaxial

310   experiments in Quane and Russell 2005; Heap et al. 2015), which we account for via the

311   Trouton ratio. This gives us some confidence that, under minor local shearing within a system

312   that is loaded anisotropically, our model is valid. Nonetheless, we note that validation for

313   shearing systems requires future systematic study over a larger range of better constrained

314   shear stress. This limitation means that our model does not, for example, explicitly predict the

315   formation of fiammé in welded ignimbrites. Secondly, the model assumes that interstitial gas

316   escapes freely from the welding system, and does not apply when gas escape is significantly

317   hindered by the permeability of the connected pore network. We can determine the conditions

318   under which this second limitation is important.

319   The characteristic lengthscale beyond which a viscous system is permeability-limited

320   is the compaction length $L_c = \left(k_r \mu / \mu_g\right)^{1/2}$ (Michaut et al. 2009; Kennedy et al. 2016), where

321   k_r is a reference permeability and μ_g is the gas viscosity. If we normalize our system length

322   by L_c we have

323

$$\bar{L} = \frac{L}{L_c} \approx L \sqrt{\frac{\mu_g}{k_r \mu}}.$$

Eq. 6

324

325 If $\bar{L} \gg 1$, permeability is a rate-limiting parameter, with the consequence that P_g may rise in

326 parts of the system and affect the welding rate (because the welding rate depends is sensitive

327 to $P_c - P_g$); this regime is termed *compaction welding*. If $\bar{L} \ll 1$, gas escape can occur more

328 rapidly than welding occurs and the process is not hindered by sluggish gas escape. The

329 analysis presented via Eqs 1-4 is therefore valid in the regime $\bar{L} \ll 1$.

330

331 **5.2 Welding regimes in nature**

332 The dimensionless length $\bar{L}$ discriminates between regimes in which welding is or is not limited

333 by permeable outgassing of the interstitial gas phase. For the non-limited regime ($\bar{L} \ll 1$) in

334 which our welding model is valid, we can also discriminate between regimes in which welding

335 is dominated by confining pressure (*pressure welding*), or by capillary pressure arising from

336 the surface tension (*capillary welding*). From Eq. 2, we see that the confining pressure term

337 dominates the capillary pressure term when

338

$$\bar{P} \gg \left(\frac{1 - \phi_i \bar{\phi}}{\bar{\phi} - \bar{\phi} \phi_i} \right)^{1/3} \quad \text{pressure welding,}$$

$$\bar{P} \ll \left(\frac{1 - \phi_i \bar{\phi}}{\bar{\phi} - \bar{\phi} \phi_i} \right)^{1/3} \quad \text{capillary welding.}$$

Eq. 7

339

340 The dependence on the porosity (via $\bar{\phi}$) arises because capillary stress always tends towards

341 infinity as bubble radius tends towards zero, such that a system that starts in the pressure

342 welding regime may end in the capillary regime with no change in the ambient conditions. The

343 value of the terms on the right hand side of Eq. 7 is equal to unity at the start of welding so, in

344   practice we use $\bar{P} \gg 1$ and $\bar{P} \ll 1$ to discriminate between pressure and capillary welding

345   regimes.

346   Given these constraints ($\bar{P}$ and $\bar{L}$), we can assess the regimes covered by some typical

347   volcanic welding scenarios. For any situation in which welding might occur, we therefore need

348   to know μ, R_i, L, and ΔP (for simplicity, we take a constant $\Gamma = 0.3 \, \text{N.m}^{-1}$ (Wadsworth et al.

349   2016), $\mu_g \approx 10^{-5} \, \text{Pa.s}$, and $k_r = k_i \approx 7 \times 10^{-12} \, \text{m}^2$ for packed particles (Wadsworth et al.

350   2017a)). For these dimensional considerations we assume that $a_i = R_i$, because there is usually

351   insufficient information provided to compute a_i explicitly, and we justify this by noting that

352   these values are typically of the same order of magnitude (Wadsworth et al. 2016). In Table 1

353   we give a compilation of estimated values for these parameters gathered from well-studied

354   welded ignimbrites, tuffisites, welded jet engine deposits, and welded obsidian pyroclasts. In

355   each case, these parameters are converted to a quantitative range of $\bar{P}$ and $\bar{L}$ that represents the

356   initial conditions for that particular system, and plotted in Figure 5. In the case of tuffisites

357   from Volcán Colima, we use the values of particle (droplet) viscosity from Kendrick et al.

358   (2016) which incorporate the effect of crystallinity.

359   We find that very few systems are in the $\bar{L} \gg 1$ (permeability limited) regime.

360   Exceptions would include welding in particularly large welded ignimbrite systems if the

361   emplacement mode is *en masse* (we give the result for the $L \le 400$ m Bad Step Tuff, for which

362    $\bar{L}$ can exceed unity). However, under the assumption of the progressive-aggradation model for

363   the sedimentation of ignimbrites (Branney and Kokelaar 1992) and an estimated, rising $L \approx 2$

364   m thick welding window (Andrews and Branney 2011), we find that $\bar{L} \ll 1$ is more typical for

365   ignimbrite emplacement. The *en masse* and progressive aggradation models for ignimbrite

366   emplacement represent upper and lower bounds on $\bar{L}$, respectively.

367   We also find that volcanic welding scenarios span the $\bar{P} = 1$ divide, implying that there

368   are cases for which pressure welding dominates ($\bar{P} > 1$) and cases for which capillary welding

369   dominates ($0 \leq |\bar{P}| < 1$). Pressure welding appears to be typical of tuffisites and ignimbrites,

370   while capillary welding appears to be typical of the formation of obsidian pyroclasts and of

371   undesirable welding in the combustion chamber of jet engines (Figure 5). Tuffisites, in

372   particular, are known to have variable and complex pressure–temperature histories, implying

373   that they may track through $\bar{P}$ space during their formation and welding (Tuffen and Dingwell

374   2005; Castro et al. 2012; Saubin et al. 2016). If the exact evolution of pressure and temperature

375   were known, then our model could be used to determine the degree of welding throughout.

376   For each of the cases presented in Figure 5, we can compute a timescale for the porosity

377   to reach the equilibrium value $\phi = \phi_c$. For systems welding at any $\bar{P}$, for $\bar{L} \ll 1$, this timescale

378   includes contributions from the pressure and capillary components, and can be taken as the

379   reciprocal of the sum of the characteristic welding rates associated with the confining pressure

380   and capillary pressure terms

381

$$\lambda_W \approx \left(\frac{\Delta P}{\langle \mu \rangle} + \frac{\Gamma}{\langle \mu \rangle \langle R_i \rangle} \right)^{-1}.$$

Eq. 8

382

383   We use Eq. 8 and the inputs in Table 1 to compute λ_W (in seconds) for each case study example

384   given. We find that most systems weld over a timescale of 1 second to 1 day. Exceptions,

385   which require very long timescales to weld, are crystal-rich tuffisites (Kendrick et al. 2016) or

386   obsidian pyroclasts welding under the lowest temperature and gas pressure conditions expected

387   (Gardner et al. 2017). In both of those slow-welding scenarios, it is unlikely that welding will

388   complete before other processes, such as cooling of the particles or deposit, terminate welding.

389   However, remarkably, the welding timescale for most rhyolitic systems investigated appears

390   to span a similar range regardless of the $\bar{P}$ of formation; hence $\langle \mu \rangle$, and therefore the degassing

391 and temperature history, is the most important controlling parameter in welding for rhyolitic

392 magmas.

393

5.3 User-friendly computational tools for solving welding problems in volcanic scenarios in Python™ and Excel™

394

395

396 As part of this contribution, we provide a downloadable executable file for Linux™ and Mac

397 platforms, which solves the full diffusion–welding problem given here. The executable

398 requires the following user inputs: particle size distribution (as a .txt or .csv file), initial

399 porosity ϕ_i, initial dissolved water concentration C_i, initial temperature, gas pressure P_g,

400 pressure differential $\Delta P = P_l - P_g$, surface tension Γ, and the spatial resolution for the

401 diffusion solution (we set a default value of 100 steps, which is sufficient for most cases). We

402 additionally allow the user to input a temperature rate, which should be positive for heating,

403 negative for cooling, or zero for isothermal conditions, and which imposes a linear change in

404 temperature. The outputs of this code are the monodisperse or polydisperse solutions for

405 porosity as a function of time and the value of $\langle C \rangle$. Similarly, we provide an editable Excel™

406 sheet for solving our welding code for isothermal or non-isothermal conditions including for

407 polydisperse particles (or droplets), but without diffusion of volatiles. This code is available

408 via VHub (https://vhub.org/resources/4568).

409

410

6   Concluding remarks

411

412 We present a universal theoretical model of welding of natural volcanic material at relevant

413 volcanic conditions. The model includes the complex effect of syn-welding dehydration,

414 accounts for the effects of confining pressure and capillary pressure, and is valid for both

415   isothermal and non-isothermal conditions. The welding model is grounded in the microphysical

416   behaviour of a welding system, and requires no fitting parameters.

417   We use scaling arguments to assess the validity of the model for natural welding

418   scenarios, and conclude that it can be applied to welding in tuffisites, in volcanic conduits, at

419   the base of aggrading pyroclastic density currents, and in jet engines. Our model predicts that

420   volcanic systems span the divide between the regime in which the capillary stress at particle

421   walls drives welding, and the regime in which the driving pressure for welding is the difference

422   between the liquid and the interstitial gas pressures. We find that in most cases examined here,

423   the permeability of the interstitial gas phase does not limit the welding dynamics. Finally, we

424   find that the total time required for complete welding spans seconds to years, and that the

425   viscosity of the particles, or the evolution of viscosity during particle degassing, is the most

426   variable parameter in nature.

427   The model we present provides a flexible and general tool for investigating welding

428   phenomena across a wide range of volcanically-relevant scenarios. The model solution is given

429   for the specific case of rhyolite welding via a vHub resource.

430

431

445

Author contributions to this work

447 The team at the TOMCAT beamline (PSI, Switzerland) included F.B. Wadsworth (team lead),

448 J. Vasseur, E.W. Llewellin, K.J. Dobson, F.W. von Aulock, J. Fife, and F. Marone. J. Schauroth

449 and K.J. Dobson processed the 3D datasets and extracted raw data. F.B. Wadsworth, J. Vasseur,

450 and E.W. Llewellin performed the analysis and model development. F.B. Wadsworth, J.

451 Schauroth, J.E. Gardner, K.-U. Hess, M.J. Heap, H. Tuffen, and D.B. Dingwell provided

452 additional *ex situ* or calibration data for analysis and consulted on the data treatment and the

453 manuscript. F.B. Wadsworth, J. Schauroth, and E.W. Llewellin led the drafting of a manuscript

454 text with help from all authors. T. Havard compiled data from natural deposits.

455

456

457 References cited

458
459
460 Andrews GDM, Branney MJ (2011) Emplacement and rheomorphic deformation of a large,

461   lava-like rhyolitic ignimbrite: Grey's Landing, southern Idaho. Geol Soc Am Bull

462   123:725–743. doi: 10.1130/b30167.1

463 Branney M, Kokelaar Bp, McConnell B (1992) The Bad Step Tuff: a lava-like rheomorphic

464   ignimbrite in a calc-alkaline piecemeal caldera, English Lake District. Bull Volcanol

465   54:187–199. doi: 10.1007/BF00278388

466 Branney M, Kokelaar P (1992) A reappraisal of ignimbrite emplacement: progressive

467   aggradation and changes from particulate to non-particulate flow during emplacement of

468   high-grade ignimbrite. Bull Volcanol 54:504–520. doi: 10.1007/BF00301396

469 Castro JM, Bindeman IN, Tuffen H, Ian Schipper C (2014) Explosive origin of silicic lava:

470   Textural and δD-H2O evidence for pyroclastic degassing during rhyolite effusion. Earth

471   Planet Sci Lett 405:52–61. doi: 10.1016/j.epsl.2014.08.012

472 Castro JM, Cordonnier B, Tuffen H, et al (2012) The role of melt-fracture degassing in

473   defusing explosive rhyolite eruptions at volcán Chaitén. Earth Planet Sci Lett 333:63–

474   69. doi: http://dx.doi.org/10.1016/j.epsl.2012.04.024

475 Cimarelli C, Yilmaz T, Colombier M, et al (2017) Micro-and nano-CT textural analysis of an

476   experimental volcanic fulgurite. EGU Gen Assem Conf Abstr 19:17982

477 Clarke AB, Voight B (2000) Pyroclastic current dynamic pressure from aerodynamics of tree

478   or pole blow-down. J Volcanol Geotherm Res 100:395–412. doi: 10.1016/S0377-

479   0273(00)00148-7

480 Elam WT, Kerstein AR, Rehr JJ (1984) Critical properties of the void percolation problem

481   for spheres. Phys Rev Lett 52:1516

482 Fife JL, Rappaz M, Pistone M, et al (2012) Development of a laser-based heating system for

483   in situ synchrotron-based X-ray tomographic microscopy. J Synchrotron Radiat 19:352–

484   358

485   Frenkel J (1945) Viscous flow of crystalline bodies under the action of surface tension. J

486   Phys 9:385–391

487   Friedman I, Long W, Smith RL (1963) Viscosity and water content of rhyolite glass. J

488   Geophys Res 68:6523–6535

489   Gardner JE, Llewellin EW, Watkins JM, Befus KS (2017) Formation of obsidian pyroclasts

490   by sintering of ash particles in the volcanic conduit. Earth Planet Sci Lett 459:252–263.

491   doi: 10.1016/J.EPSL.2016.11.037

492   Gardner JE, Wadsworth FB, Llewellin EW, et al (2018) Experimental sintering of ash at

493   conduit conditions and implications for the longevity of tuffisites. Bull Volcanol 80:23.

494   doi: 10.1007/s00445-018-1202-8

495   Gardner JE, Wadsworth FB, Llewellin EW, et al (2019) Experimental constraints on the

496   textures and origin of obsidian pyroclasts. Bull Volcanol 81:22. doi: 10.1007/s00445-

497   019-1283-z

498   Giachetti T, Gonnermann HM (2013) Water in volcanic pyroclast: Rehydration or incomplete

499   degassing? Earth Planet Sci Lett 369–370:317–332. doi: 10.1016/J.EPSL.2013.03.041

500   Giehl C, Brooker R, Marxer H, Nowak M (2016) An experimental simulation of volcanic ash

501   deposition in gas turbines and implications for jet engine safety. Chem Geol

502   Giordano D, Russell JK, Dingwell DB (2008) Viscosity of magmatic liquids: a model. Earth

503   Planet Sci Lett 271:123–134

504   Gonnermann HM, Manga M (2003) Explosive volcanism may not be an inevitable

505   consequence of magma fragmentation. Nature 426:432–435

506   Gottsmann J, Giordano D, Dingwell DB (2002) Predicting shear viscosity during volcanic

507   processes at the glass transition: a calorimetric calibration. Earth Planet Sci Lett

508   198:417–427

509 Grunder AL, Laporte D, Druitt TH (2005) Experimental and textural investigation of

510   welding: effects of compaction, sintering, and vapor-phase crystallization in the rhyolitic

511   Rattlesnake Tuff. J Volcanol Geotherm Res 142:89–104. doi:

512   http://dx.doi.org/10.1016/j.jvolgeores.2004.10.018

513 Heap MJ, Farquharson JI, Wadsworth FB, et al (2015) Timescales for permeability reduction

514   and strength recovery in densifying magma. Earth Planet Sci Lett 429:223–233. doi:

515   10.1016/j.epsl.2015.07.053

516 Hess KU, Cordonnier B, Lavallee Y, Dingwell DB (2007) High-load, high-temperature

517   deformation apparatus for synthetic and natural silicate melts. Rev Sci Instrum

518   78:75102. doi: 10.1063/1.2751398

519 Hess KU, Dingwell DB (1996) Viscosities of hydrous leucogranitic melts: A non-Arrhenian

520   model. Am Mineral 81:1297–1300

521 Hess KU, Dingwell DB, Webb SL (1995) The influence of excess alkalis on the viscosity of

522   a haplogranitic melt. Am Mineral 80:297–304

523 Kendrick JE, Lavallée Y, Varley NR, et al (2016) Blowing off steam: Tuffisite formation as a

524   regulator for lava dome eruptions. Front Earth Sci 4:. doi: 10.3389/feart.2016.00041

525 Kennedy BM, Wadsworth FB, Vasseur J, et al (2016) Surface tension driven processes

526   densify and retain permeability in magma and lava. Earth Planet Sci Lett 433:116–124.

527   doi: 10.1016/j.epsl.2015.10.031

528 Liu Y, Zhang Y, Behrens H (2005) Solubility of H_2O in rhyolitic melts at low

529   pressures and a new empirical model for mixed H_2O–CO_2

530   solubility in rhyolitic melts. J Volcanol Geotherm Res 143:219–235

531 Lu B, Torquato S (1992) Nearest-surface distribution functions for polydispersed particle

532   systems. Phys Rev A 45:5530

533 Mackenzie JK, Shuttleworth R (1949) A phenomenological theory of sintering. Proc Phys

534   Soc Sect B 62:833

535   McIntosh IM, Llewellin EW, Humphreys MCS, et al (2014) Distribution of dissolved water

536   in magmatic glass records growth and resorption of bubbles. Earth Planet Sci Lett

537   401:1–11. doi: 10.1016/j.epsl.2014.05.037

538   Michaut C, Bercovici D, Sparks RSJ (2009) Ascent and compaction of gas rich magma and

539   the effects of hysteretic permeability. Earth Planet Sci Lett 282:258–267

540   Mueller SP, Helo C, Keller F, et al (2018) First experimental observations on melting and

541   chemical modification of volcanic ash during lightning interaction. Sci Rep 8:1389. doi:

542   10.1038/s41598-018-19608-3

543   Olevsky EA (1998) Theory of sintering: from discrete to continuum. Mater Sci Eng R

544   Reports 23:41–100

545   Prado M, Dutra Zanotto E, Müller R (2001) Model for sintering polydispersed glass particles.

546   J Non Cryst Solids 279:169–178

547   Prousevitch AA, Sahagian DL, Anderson AT (1993) Dynamics of diffusive bubble growth in

548   magmas: isothermal case. J Geophys Res Solid Earth 98:22283–22307. doi:

549   10.1029/93JB02027

550   Quane SL, Russell JK (2005a) Welding: insights from high-temperature analogue

551   experiments. J Volcanol Geotherm Res 142:67–87. doi:

552   http://dx.doi.org/10.1016/j.jvolgeores.2004.10.014

553   Quane SL, Russell JK (2005b) Ranking welding intensity in pyroclastic deposits. Bull

554   Volcanol 67:129–143

555   Riehle JR (1973) Calculated Compaction Profiles of Rhyolitic Ash-Flow Tuffs. Bull Geol

556   Soc Am 84:2193–2216. doi: 10.1130/0016-7606(1973)84<2193:CCPORA>2.0.CO;2

557   Russell JK, Quane SL (2005) Rheology of welding: inversion of field constraints. J Volcanol

558   Geotherm Res 142:173–191. doi: http://dx.doi.org/10.1016/j.jvolgeores.2004.10.017

559 Rust AC, Cashman K V, Wallace PJ (2004) Magma degassing buffered by vapor flow

560   through brecciated conduit margins. Geology 32:349–352

561 Ryan AG, Russell JK, Nichols ARL, et al (2015) Experiments and models on H2O retrograde

562   solubility in volcanic systems. Am Mineral 100:774–786. doi: 10.2138/am-2015-5030

563 Saubin E, Tuffen H, Gurioli L, et al (2016) Conduit Dynamics in Transitional Rhyolitic

564   Activity Recorded by Tuffisite Vein Textures from the 2008–2009 Chaitén Eruption.

565   Front Earth Sci 4:. doi: 10.3389/feart.2016.00059

566 Sparks RSJ, Tait SR, Yanev Y (1999) Dense welding caused by volatile resorption. J Geol

567   Soc London 156:217–225. doi: 10.1144/gsjgs.156.2.0217

568 Streck MJ, Grunder AL (1995) Crystallization and welding variations in a widespread

569   ignimbrite sheet; the Rattlesnake Tuff, eastern Oregon, USA. Bull Volcanol 57:151–169

570 Sumner JM, Branney MJ (2002) The emplacement history of a remarkable heterogeneous,

571   chemically zoned, rheomorphic and locally lava-like ignimbrite: 'TL' on Gran Canaria.

572   J Volcanol Geotherm Res 115:109–138. doi: 10.1016/S0377-0273(01)00311-0

573 Tuffen H, Castro JM (2009) The emplacement of an obsidian dyke through thin ice:

574   Hrafntinnuhryggur, Krafla Iceland. J Volcanol Geotherm Res 185:352–366

575 Tuffen H, Dingwell D (2005) Fault textures in volcanic conduits: evidence for seismic trigger

576   mechanisms during silicic eruptions. Bull Volcanol 67:370–387. doi: 10.1007/s00445-

577   004-0383-5

578 Tuffen H, Dingwell DB, Pinkerton H (2003) Repeated fracture and healing of silicic magma

579   generate flow banding and earthquakes? Geology 31:1089–1092. doi: 10.1130/g19777.1

580 Vasseur J, Wadsworth FB (2017) Sphere models for pore geometry and fluid permeability in

581   heterogeneous magmas. Bull Volcanol 79:. doi: 10.1007/s00445-017-1165-1

582 Vasseur J, Wadsworth FB, Lavallée Y, et al (2013) Volcanic sintering: Timescales of viscous

583   densification and strength recovery. Geophys Res Lett 40:5658–5664. doi:

584   10.1002/2013GL058105

585   Wadsworth FB, Vasseur J, Aulock FW, et al (2014) Nonisothermal viscous sintering of

586   volcanic ash. J Geophys Res Solid Earth 119:8792–8804

587   Wadsworth FB, Vasseur J, Llewellin EW, et al (2016) Sintering of viscous droplets under

588   surface tension. Proc R Soc A Math Phys Eng Sci 472:20150780. doi:

589   10.1098/rspa.2015.0780

590   Wadsworth FB, Vasseur J, Llewellin EW, et al (2017a) Topological inversions in coalescing

591   granular media control fluid-flow regimes. Phys Rev E 96:. doi:

592   10.1103/PhysRevE.96.033113

593   Wadsworth FB, Vasseur J, Llewellin EW, Dingwell DB (2017b) Sintering of polydisperse

594   viscous droplets. Phys Rev E 95:033114. doi: 10.1103/PhysRevE.95.033114

595   Walker GPL (1983) Ignimbrite types and ignimbrite problems. J Volcanol Geotherm Res

596   17:65–88. doi: 10.1016/0377-0273(83)90062-8

597   Wright HM, Cashman K V (2014) Compaction and gas loss in welded pyroclastic deposits as

598   revealed by porosity, permeability, and electrical conductivity measurements of the

599   Shevlin Park Tuff. Geol Soc Am Bull 126:234–247. doi: 10.1130/b30668.1

600   Zhang Y, Ni H (2010) Diffusion of H, C, and O components in silicate melts. Rev Mineral

601   Geochemistry 72:171–225

602

603

Table 1 Constraints underpinning $\bar{P}$ and $\bar{L}$ from natural deposits or scenarios

	Particle viscosity[#] μ (Pa.s)	System length L (m)	Particle radius[$] R_i (m)	Liquid pressure P_l (Pa)	Gas pressure P_g (Pa)	Initial water content[**] C_i (wt.%)	Emplacement temperature[**] T (K)	References
Welded ignimbrites								
Bad Step Tuff	10^7-10^8	40-400[*]	10^{-5}-10^{-3}	10^6-10^7	10^5-10^6	0.1-0.2	1273	(Branney et al. 1992)
TL	10^5-10^6	10.4-28[*]	10^{-5}-10^{-3}	3.1-7.5x10^5	10^5-10^6	0.47-0.87	1084-1183	(Sumner and Branney 2002)
Grey's Landing	10^7-10^9	2-70[*]	10^{-5}-10^{-3}	10^5-10^6	10^5-10^6	0.1-0.2	1198-1298	(Andrews and Branney 2011)
Rattlesnake tuff	10^8-10^{10}	15-70[*]	10^{-5}-10^{-3}	4.1x10^5-10^6	10^5-10^6	0.1-0.2	1073-1153	(Streck and Grunder 1995)
Tuffisites								
Chaitén (2008)	10^7-10^9	0.005-0.03	1.25x10^{-4}-2.5x10^{-4}	10^6-10^7	4.6x10^6-8.1x10^6	0.44-1.2	1023-1098	(Castro et al. 2012; Saubin et al. 2016)
Cordon Caulle 2011-2013	10^8-10^9	0.005-0.03	10^{-6}-10^{-3}	10^6-10^7	4.6x10^6-8.1x10^6	0.16-0.25	1168	(Castro et al. 2014)
Colima	10^{10}-10^{11}	0.001-0.05	10^{-4}-10^{-3}	10^5-10^6	10^5	0.1-0.2	1213-1253	(Kendrick et al. 2016)
Törfajökull	10^9-10^{14}	0.001-0.05	10^{-5}-10^{-3}	10^6-10^7	4.6x10^6-8.1x10^6			(Tuffen and Dingwell 2005)
Obsidian pyroclasts								
Mono craters	10^6-10^{12}	0.01-0.02	2x10^{-5}-1.7x10^{-4}	1.002x10^5	10^5			(Gardner et al. 2017)
Jet engine deposits								
Rhyolitic experimental	10^3-10^9	10^{-3}-10^{-2}	3x10^{-5}	4.0002x10^6	4x10^6	0.1	1148-1848	(Giehl et al. 2016)

[#]The viscosity is either taken from the references for each case study or otherwise is calculated using *Hess and Dingwell*, [1996] with the C_i and T given for most cases (exceptions are the TL ignimbrite and the basaltic example for the jet engine deposits, both of which are calculated using *Giordano et al.*, [2008] and the composition given in the references; for TL, we use the WTL trachyte zone composition because this is the 'lava like' facies (Sumner and Branney 2002)).

[*]This system length is assuming *en masse* deposition, but for progressive aggradation we take 2 m for all ignimbrites

[+]We take this liquid pressure to be the hydrostatic loading pressure assuming a density of 2300 kg.m^{-3}. Except for the tuffisite cases, the gas pressure is added to the liquid pressure.

[£]The upper limit of these gas pressures is given by estimates of dynamic pressures during transport in pyroclastic density currents (Clarke and Voight 2000).

[**]Note that these parameters are only required if the viscosity is not given directly by the originating authors. The value for C_i is approximated as 0.1-0.2 wt.% if other information is not given.

[$]We make the simplifying assumption that $a_i = R_i$ for this scaling analysis.

604
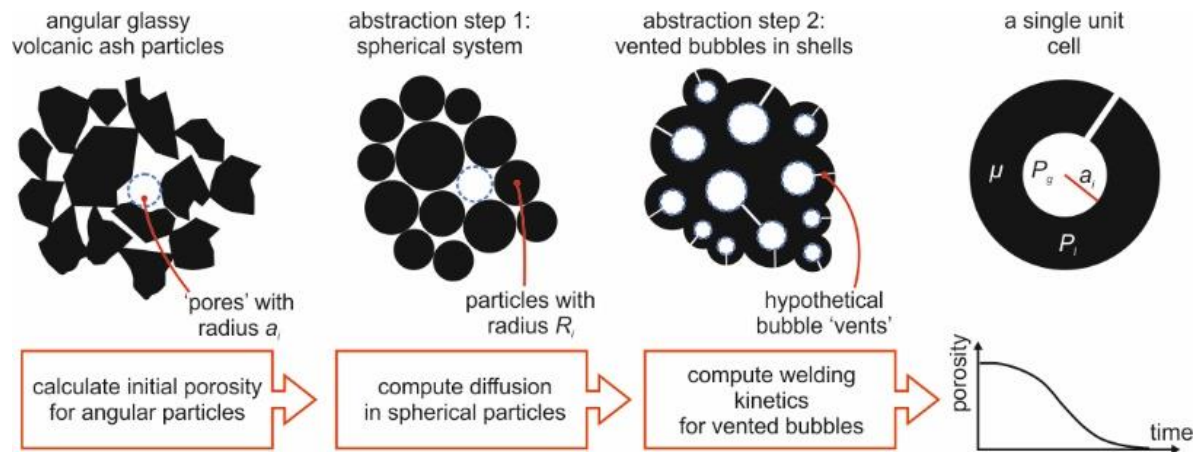
Figure 1. The development of a diffusion–welding model. The natural system is composed of angular volcanic particles, which are abstracted to a pack of spherical particles with the same initial porosity. The diffusion model is used (Eq. 3) to compute the average water content as a function of time $\langle C \rangle (R_i, t)$, which is converted to an average viscosity $\langle \mu \rangle$. Then we make a further abstraction to vented bubble geometry and the welding is computed in terms of an evolution of the total porosity with time $\phi(t)$ using Eqs 1-2, accounting for the polydispersivity of the initial particle size distribution (Wadsworth et al. 2017b).

613
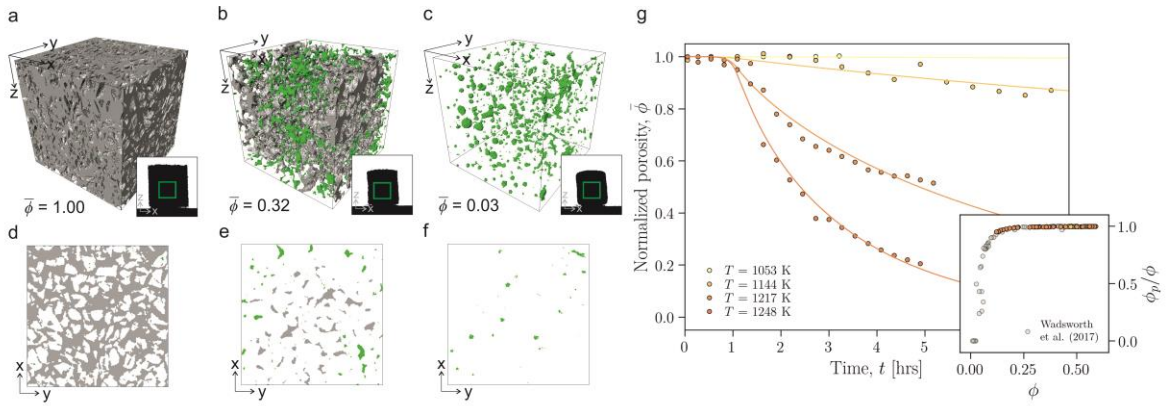
614

615 [Full page width]

616 **Figure 2.** Constraints of time-dependent welding collected *in situ* using either optical

617 dilatometry or x-ray tomography. **a-c**, 3-dimensional rendered images of the time-dependent

618 welding process segmented on the basis of grayscale gradient filtering from continuous, time-

619 resolved, *in situ* x-ray tomography data. The particle phase is rendered transparent, and the

620 pore phase is divided into a grey and a green component depending on whether it is connected

621 across the sample in any direction (grey) or is isolated from connections (green). Box edge

622 lengths of the sub-volume displayed are 350 μm. Displayed is one representative experiment

623 performed at $T = 1350$ K, for which the dimensionless porosity $\bar{\phi}$ is labelled. Inset in each

624 panel is the 2-dimensional side-view of an initially cylindrical sample from an experiment at

625 the same conditions performed in the optical dilatometer (image base length of 5 mm). **d-f**, a

626 2-dimensional horizontal slice through each of the 3-dimensional rendered images in **a-c** taken

627 at the midpoint of the z-axis in the sample. **g**, The porosity as a function of time of the obsidian

628 particles sintered *in situ* using time-resolved x-ray tomography at a range of temperatures

629 (labelled). The curves represent the solutions to Eqs 1 or 2 with $\bar{P} = 0$ and computing the

630 time-dependent diffusion of volatiles out of the particles (Eq. 4). *Inset:* the connectivity of the

631 pore phase with porosity showing the collapse from fully connected to isolated as $\phi \rightarrow \phi_c$

30

632   during welding. Data are compared with welding in synthetic glass systems (Wadsworth et al.

633   2017a).

634

635
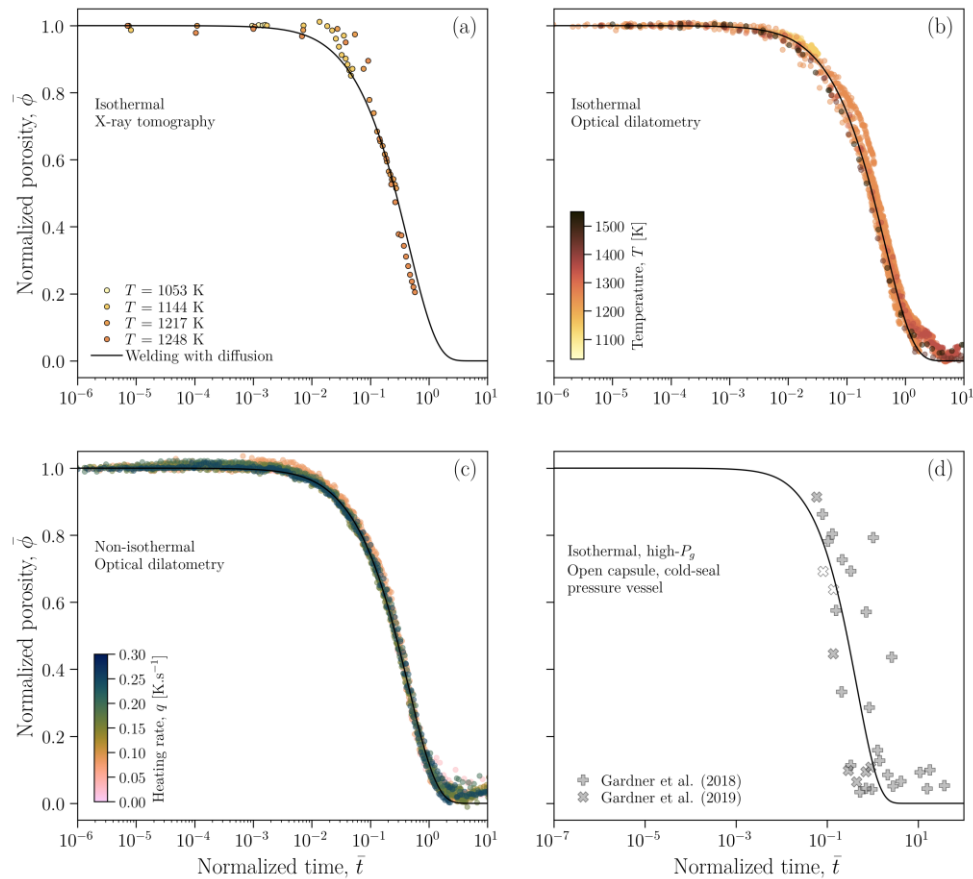
Figure 3. Modeling the evolution of the pore phase between the welding droplets. **a**, the porosity $\bar{\phi}$ as a function of time for each experimental T for the x-ray tomography experiments only. These data are compared with the results of Eq. 2 (welding) with Eq. 4 (diffusion), which account for syn-welding degassing of the droplets and which require no fitting parameters. These data are the same as those presented in Figure 2g. **b**, the same as **a** but for the data collected using optical dilatometry (i.e. without 3-dimensioanl microstructural information) showing that this technique can be used to capture the bulk decay of porosity with time. **c**, the same dimensionless plot as in **b** but for non-isothermal experiments at different experimental heating rates, showing that regardless of the $T(t)$ path taken by the samples, the efficacy of our model (Eqs 4-6) is robust. In all panels, the dimensionless time is given by Eq. 3. **d**, The data from Gardner et al. (2018) and Gardner et al. (2019) collected using a high-P_g cold seal vessel, re-analysed using the diffusion-welding model given here. The filled points represent data for

32

650   which rhyolite particles are hydrating (from $C_i = 0.15$ wt.% to equilibrium conditions at high

651   P_g and high T) while welding, and the un-filled points represent data for which rhyolite particles

652   are de-hydrating (from $C_i = 2.3$ wt.% to equilibrium conditions at high P_g and high T). See the

653   papers originating the data for more information.

654

655
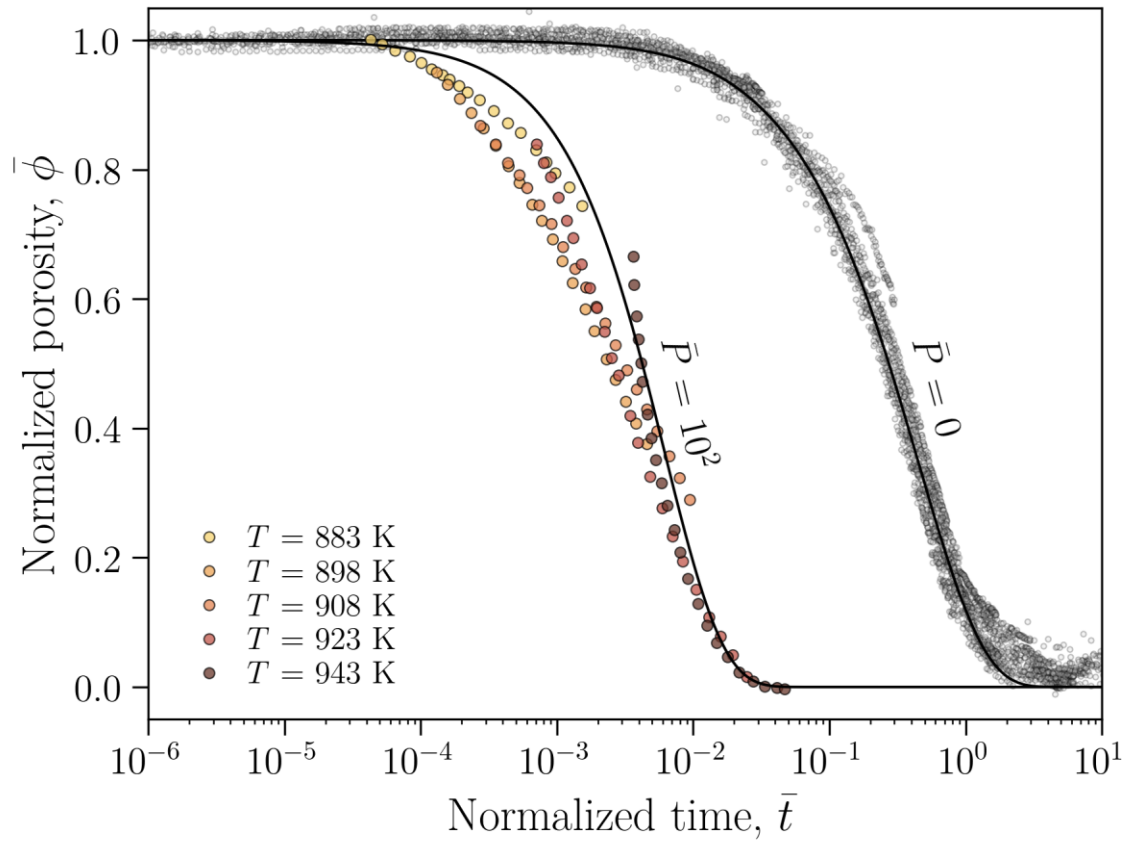
656

657 [half-page width or less]

658 **Figure 4.** The effect of pressure on the welding of glassy particles. Shown here are data from

659 *Friedman et al.*, [1963], in which synthetic glass particles (Pyrex™) are welded under a

660 pressure equivalent to $\bar{P} = 100$, and at a range of temperatures (labelled). We use the values

661 of μ, R_i and P_l given in their work, and the curve represents the solution to Eq. 2 without fitting

662 parameters. Shown for reference is the solution for $\bar{P} = 0$ and all data from Figure 3 given in

663 grey. In all cases, the dimensionless time is given by Eq. 3.

664

665

666

667

668
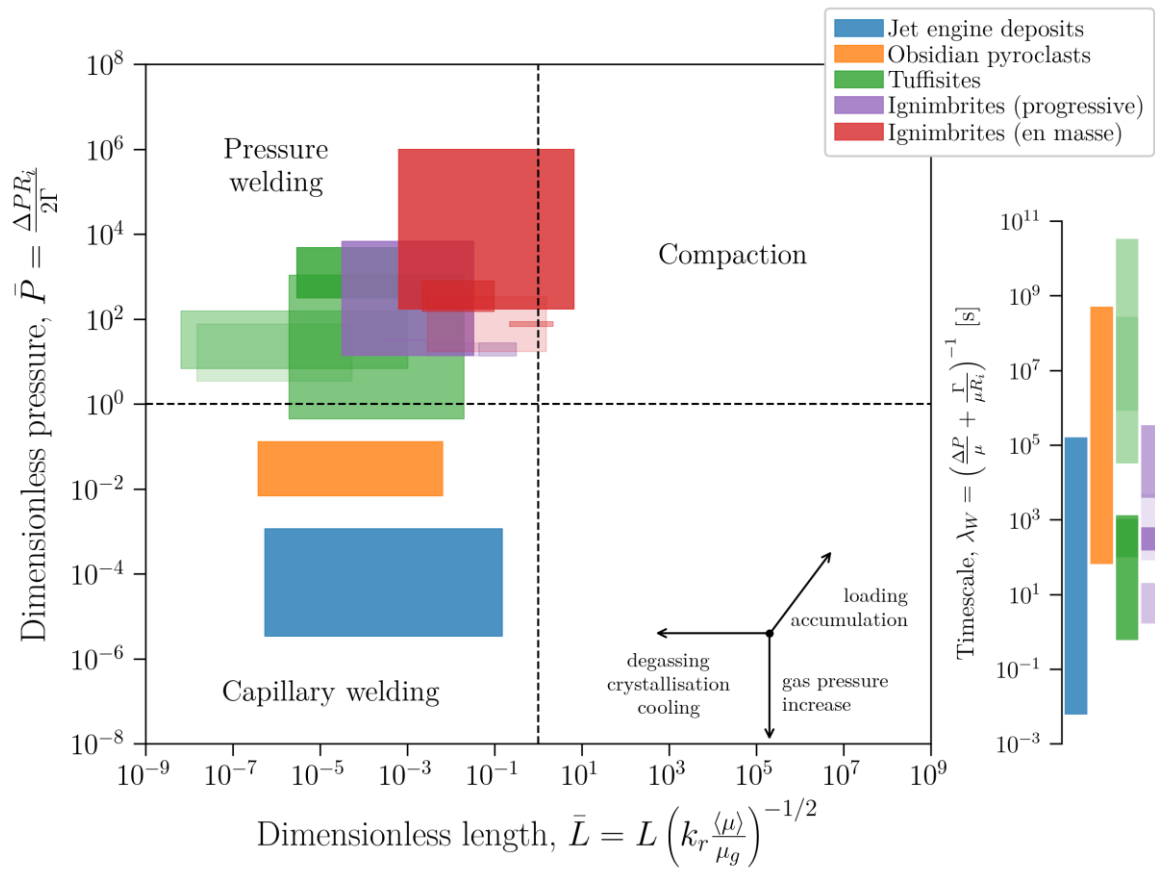
[1/2 page width or less]

Figure 5. Scenarios and regimes for volcanic welding. A plot of $\bar{P}$ and $\bar{L}$ regimes for volcanic welding with the range of conditions for natural examples given using constraints compiled in Table 1.